Atomic Spectroscopy

Article

A Rapid Method for Preparing Hematite Reference Material for *In-situ* Determination of Iron Isotope Ratios

Xianli Zeng,[a,d] Ming Li,[a,*] Hongyun Jin,[b] Zhiwen Cao,[b,d] Detao He,[c] Zhaochu Hu,[a,b] Yongsheng Liu,[c] and Xinna Chai[d]

[a] State Key Laboratory of Geological Processes and Mineral Resources, China University of Geosciences, Wuhan 430074, P. R. China

[b] Faculty of Materials Science and Chemistry, China University of Geosciences, Wuhan 430074, P. R. China

[c] School of Earth Sciences, China University of Geosciences, Wuhan 430074, P. R. China

[d] Graduate School, China University of Geosciences, Wuhan 430074, P. R. China

Received: *March 29, 2024;* ***Revised:*** *December 16, 2024;* ***Accepted:*** *December 19, 2024;* ***Available online:*** *December 19, 2024.*

DOI: 10.46770/AS.2024.053

ABSTRACT: The advent of laser ablation multi-collector inductively coupled plasma mass spectrometry (LA-MC-ICP-MS) has opened new avenues for investigating iron isotope cycling across various temporal and spatial scales in biological and geological processes. However, accurate and precise measurements of iron isotopes in hematite have been hindered by the lack of matrix-matched reference materials. In this study, we developed hematite reference materials (RMs) by combining nanopowder pelletization and solid-phase sintering techniques. Nano-Fe_2O_3 powder was compressed into pellets and subsequently sintered at 1000°C for 120 min. This method produced stable targets with sufficient mechanical strength suitable for in-situ analysis. The prepared hematite exhibited excellent cohesion, smooth surfaces, and dense structures, making it highly suitable for laser ablation analysis. We demonstrated the homogeneity of iron isotopic composition through repeated measurements using LA-MC-ICP-MS. The $\delta^{56}Fe_{IRMM014}$ values for the initial powder, sintered pellets, and unsintered pellets were 0.45 ± 0.04‰ (2SD, N=20), 0.44 ± 0.04‰ (2SD, N=21), and 0.45 ± 0.02‰ (2SD, n=3), respectively, indicating high consistency. The integration of pressed powder pellet techniques with high-temperature sintering provides a rapid and convenient method for developing matrix-matched RMs. This approach shows potential for creating diverse matrix-matched reference materials for various analytical applications.

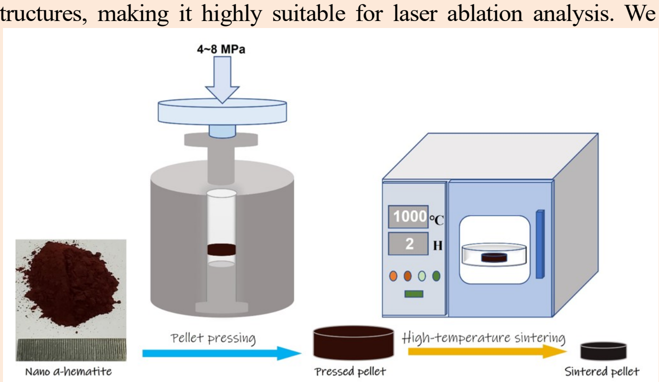

INTRODUCTION

Iron (Fe) is one of the most abundant elements in the solar system and serves as a redox-sensitive element that has been biologically harnessed since the inception of life.[1,2] Iron has four stable isotopes: ^{54}Fe, ^{56}Fe, ^{57}Fe, and ^{58}Fe, with relative abundances of approximately 5.84%, 91.76%, 2.12%, and 0.28%, respectively.[3] The isotopic fractionation of iron offers a promising tool for investigating diverse geological processes in Earth and planetary sciences.[4-7] Hematite (α-Fe_2O_3) is the most stable and widely distributed red iron oxide mineral in nature, making it a subject of great interest to geologists.[8] It is generally acknowledged that hematite plays an indispensable role in the iron cycle, paleoclimate reconstructions, and past redox conditions.[9,10] Existing approaches for Fe isotope analysis primarily include thermal ionization mass spectrometry (TIMS)[11] and multi-collector inductively coupled plasma-mass spectrometry (MC-ICP-MS)[7,12] for bulk analysis, as well as LA-MC-ICP-MS and secondary ionization mass spectrometry (SIMS)[13] for *in-situ* and microanalysis. Among these methods, *in-situ* Fe isotope analysis stands out as an intriguing avenue for investigating intricate geological processes due to its simple pretreatment process and the ability to perform non-destructive analysis of samples on the micron scale.[14-18]

As all other isotopes analyzed by LA-MC-ICP-MS, *in-situ* Fe isotope measurement has been hindered by matrix effects. These effects manifest in various processes within LA-MC-ICP-MS, such as differences in crater depth, aerosol particle size, and mass yield during laser ablation, which introduce primary matrix effects that affect the accuracy and precision of iron isotope measurements.[19,20] Additionally, vaporization and ionization of ablated particles within the ICP also contribute to matrix effects.[12,21-23] For accurate *in-situ* Fe isotope analysis, matrix-matched calibration standards are essential. However, suitable Fe oxide reference materials are currently limited. While IRMM014 and IRMM524A have been traditionally used as reference materials for *in-situ* Fe isotope analysis, IRMM014 is now depleted and no longer commercially available.[24,25] This shortage of matrix-matched Fe oxide reference materials presents a significant challenge for high-precision Fe isotope microanalysis.

The urgent task at hand is to produce substantial quantities of matrix-matched reference materials. Several approaches have been developed for reference material preparation: 1) Chemical synthesis of single-phase minerals; 2) Selection and verification of naturally homogeneous minerals; 3) Production of fused glasses through high-temperature melting; 4) Preparation of pressed powder pellets using pulverized natural or synthetic materials. The method of pressed powder pellets is comparatively more convenient and efficient when compared to the first three methods, but the prepared samples often have poor density, making them difficult for prolonged utilization. Recent years have witnessed considerable advances in optimizing powder pelletization methods for the preparation of reference materials, which are crucial for both elemental and isotopic analytical applications. Wohlgemuth-Ueberwasser *et al.*[26] successfully synthesized a standard material, $(Fe, Ni, Cu)_{1-x}S$, by subjecting Fe, Ni, and Cu metal powders along with elemental S to high temperature and pressure. Feng *et al.*[27] also prepared nano-FeS_2 powder and subsequently compressed them into powder pellets for isotope analysis of sulfur and lead. A challenge arose with powder pellets produced through simple pressing due to their loose and fragile nature, making long-term preservation difficult. To address this issue, high-temperature techniques have been employed. For instance, Feng *et al*.[28] developed a pyrite material using plasma-activated sintering (PAS) at 600°C, while Ballhaus and Sylvester[29] synthesized materials at 950°C and a pressure of 1 GPa over a period of 2 days. Despite these methods being effective for preparing reference materials, they require specific preparation or instruments, hindering mass production.

This study aims to develop a rapid and scalable method for preparing bulk reference materials with long-term stability and utility. We present an efficient protocol that combines nanopowder pelletization and solid-phase sintering techniques to produce hematite reference materials specifically designed for *in-situ* Fe isotope analysis.

EXPERIMENTAL

Regents and materials. Deionized water with a resistivity of 18.0 MΩ cm was obtained from a Milli-Q water purification system (Millipore SAS, Molsheim, France). Hydrochloric acid (HCl, 36%, GR grade) and nitric acid (HNO_3, 68%, GR grade) were acquired from Sinopharm Chemical Reagent Co. Ltd and further purified using a sub-boiling distillation system. The binder polyvinyl alcohol (PVA) powder was procured from Aiweixin Chemical Process Technology Co., Ltd (Tianjin, China). Nano-sized α-Fe_2O_3 powder (30 nm, 99.5% purity, purchased from Aladdin Biochemical Technology Co., Ltd.) was used as the starting material for hematite pellet preparation. For solution Fe isotope analysis, the international Fe isotopic standard reference material IRMM-014[30] (pure iron, 99.9% purity), provided by the Institute for Reference Materials and Measurements (IRMM) of the European Commission, was employed as the external standard.

Preparation protocol. This experimental work was conducted at the State Key Laboratory of Geological Processes and Mineral Resources (GPMR), China University of Geosciences, Wuhan. The preparation protocol for solid hematite reference materials consisted of a two-step process involving pellet pressing and high-temperature sintering. Initially, nano-Fe_2O_3 powder was homogeneously blended with a polyvinyl alcohol (PVA) binder in an agate mortar. The binder solution was prepared by dissolving PVA in deionized water to achieve a concentration of 5 *wt*%. A precise mixing ratio of 1 g nano-Fe_2O_3 powder to 1 mL binder solution was maintained to obtain a homogeneous paste-like mixture. The resultant paste-like mixture underwent continuous grinding in the agate mortar until completely dry, ensuring homogeneous dispersion of PVA throughout the nano-Fe_2O_3 particles. Subsequently, 450 mg of the homogenized powder was compressed into a pellet using a 12 mm diameter die under a pressure of approximately 6 MPa for 5 minutes. The compressed pellet was then placed on a high-purity alumina porcelain boat ($Al_2O_3 \geq 99.99\%$) and subjected to thermal treatment in a muffle furnace at 1000 °C for 2 hours. The sintering process effectively enhanced the mechanical strength and stability of the pellets, making them suitable for direct LA-MC-ICP-MS analysis. Using this optimized protocol, we successfully prepared one hundred homogeneous hematite sintered pellets. The sintered pellets exhibited notable volume shrinkage and possessed sufficient mechanical strength to withstand subsequent washing and polishing treatments without cracking or fragmentation.

Analysis of major impurity elements and iron isotopes in nano-Fe_2O_3 powder. The analysis of impurity elements in nano-Fe_2O_3 powder was conducted using an Agilent 7700x Inductively Coupled Plasma Mass Spectrometer (ICP-MS) (Agilent Technologies Inc., Santa Clara, USA) at the GPMR laboratory. The analytical procedures and instrumental parameters were optimized following the established protocol developed by Li *et al*.[31]

For iron isotope characterization, measurements were performed using a Nu Plasma 1700 Multi-Collector ICP-MS (MC-ICP-MS) (Nu Instruments, Wrexham, UK) at the GPMR laboratory. This advanced instrumentation features an extended geometry with approximately 1700 mm natural dispersion, enabling superior mass resolution and efficient separation of polyatomic interference ions.[32] Two complementary analytical protocols were established for comprehensive iron isotope characterization:

In the direct testing method, 10 mg of nano-Fe_2O_3 powder underwent acid digestion in 5 mL of 20% HNO_3 at 70°C for 24 hours. Following complete dissolution, the sample was evaporated to dryness at 110°C and subsequently reconstituted in 5 mL of 2% HNO_3, maintained at 30°C for 12 hours. The resultant solution was then diluted with 2% HNO_3 to achieve a final Fe concentration of 5 μg mL^{-1} for analysis.

For the separation and purification method, 2 mL of the reconstituted solution was subjected to a comprehensive iron isotope separation and purification protocol as detailed by Lei *et al*.[33] The total procedural blank was determined to be less than 20 ng, ensuring negligible impact on the analytical results.

Bulk iron isotope analysis of sintered hematite blocks. Twenty-five randomly selected sintered block samples underwent bulk iron isotope analysis across three laboratories: the GPMR Laboratory (20 samples), the State Key Laboratory of Continental Dynamics (SKLCD) at Northwest University (3 samples), and Wuhan SampleSolution Analytical Technology Co., Ltd (SP) (2 samples). Sample collection was executed using high-purity ceramic drill bits to minimize potential contamination. The sample pretreatment protocol was identical to that established for nano-Fe_2O_3 powder analysis. GPMR and SKLCD implemented the direct testing approach, while SP employed the separation and purification protocol.

The iron isotope measurements were standardized using the standard-sample bracketing (SSB) method, with IRMM-014 certified reference solution serving as the primary calibration standard. All test solutions were systematically diluted with 2% HNO_3 to achieve a precise Fe concentration of 5.00 ± 0.25 μg g^{-1}. To ensure analytical accuracy, background corrections were performed by measuring acid blanks for 60 seconds prior to each analysis, with subsequent subtraction from sample signals. The analytical protocol comprised 25 measurement cycles, with each cycle maintaining an integration time of 8 seconds. The achieved internal precision for $^{56}Fe/^{54}Fe$ isotope ratios demonstrated high reliability, with relative standard error better than 15×10^{-6}.

***In-situ* iron isotope analysis of sintered hematite blocks.** High-precision *in-situ* iron isotope analysis of sintered hematite blocks was conducted at GPMR utilizing a NEPTUNE Plus MC-ICP-MS (Thermo Fisher Scientific, Bremen, Germany) interfaced with a NWR FemtoUC femtosecond laser ablation system (New Wave Research, Fremont, CA, USA). The analytical system was optimized with a high-capacity dry interface pump (100 m^3 h^{-1}) and enhanced with X skimmer and jet sampler cones. The Faraday collector array (L2-H2) enabled simultaneous monitoring of multiple isotopes: ^{53}Cr, ^{54}Fe, ^{56}Fe, ^{57}Fe, ^{58}Fe, and ^{60}Ni. The laser ablation system incorporated a PHAROS Yb:KGW femtosecond laser amplifier (Light Conversion Ltd., Vilnius, Lithuania), operating at an emission wavelength of 257 nm.

Table 1. Operating conditions of LA-MC-ICP-MS for *in-situ* Fe isotope analyses

Neptune Plus MC-ICP-MS	
RF Power	1200 W
Cool gas flow	16.0 L min^{-1}
Auxiliary gas flow	0.8-1.2 L min^{-1}
Argon make-up gas flow	0.6-1.0 L min^{-1}
Helium carrier gas flow	0.6-0.7 L min^{-1}
Interface cones	X skimmer cone + Jet sample cone
Instrument resolution	~8000 (high) for Fe isotope
Block number	1
Cycles of each block	120 for Fe isotope
Integration Time (s)	0.524 s
Cup-configuration	L2(^{53}Cr), L1(^{54}Fe), C(^{56}Fe), H1(^{57}Fe), H2(^{58}Fe) and H4(^{60}Ni) for Fe isotope
Laser Ablation System	
Laser type	Yb: YAG femtosecond laser
Wavelength	257 nm
Pulse length	300 fs
Energy density	~3.5 J cm^{-2}
Spot size	44 μm
Laser frequency	3 Hz

Analytical parameters were precisely controlled to ensure optimal performance: mass resolution was maintained at 8000 (5%-95% peak height definition), with laser parameters configured to a spot size of 44 μm, repetition rate of 3 Hz, and energy density of approximately 3.5 J cm^{-2}. The instrument and typical operating conditions are summarized in Table 1. Helium served as the carrier gas, and a "wet" plasma condition was established through the introduction of deionized water to effectively suppress matrix-induced effects.[12,34,35]

The iron isotope measurements were also standardized using the SSB method, with a randomly selected sintered hematite sample serving as the reference standard. Data acquisition was executed in time-resolved mode, with each analytical block comprising 120 measurement cycles at an integration time of 0.524 seconds per cycle. The measurement sequence was systematically structured with 20 seconds of background collection, followed by 35 seconds of signal acquisition, and a 7-second washout period. Comprehensive data processing and analysis were performed using the specialized ISO-Compass software platform.[36]

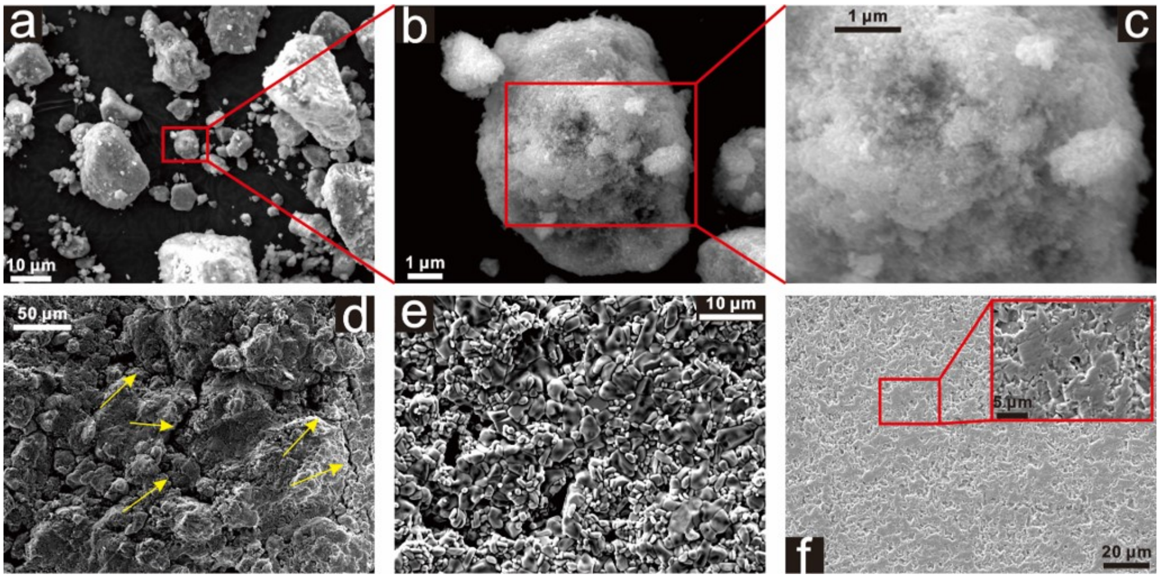

Fig. 1 SEM images: (a–c) Loosely aggregated clusters formed by 30 nm α-Fe_2O_3 powder; (d) surface cracks (indicated by yellow arrows) on an unsintered pressed hematite powder pellet; (e) hematite sintered at 1000 °C for 2 h; and (f) polished sintered hematite.

Iron isotope compositions are reported in conventional delta notation (δ) in units of per mil (‰), defined by the following equation (1):

$$\delta^{x}Fe = [({}^{x}Fe/{}^{54}Fe_{sample})/({}^{x}Fe/{}^{54}Fe_{standard})-1] \times 1000 \quad (1)$$

where x denotes the mass number 56 or 57, and IRMM-014 or the randomly selected sintered hematite sample serves as the reference standard.

Phase structure and morphological characterization. A systematic investigation of phase structure and morphological characteristics was conducted at the Faculty of Materials Science and Chemistry, China University of Geosciences (Wuhan), encompassing nano-Fe_2O_3 powder, sintered hematite blocks, and their intermediate process samples. Crystallographic phase analysis was performed using X-ray diffraction (XRD) on a Bruker AXS D8 Advance diffractometer with Cu Kα radiation (Bruker AXS GmbH, Karlsruhe, Germany). Microstructural and morphological features were characterized using high-resolution field emission scanning electron microscopy (FE-SEM) on a JEOL-JSM-IT300HR system (JEOL Ltd., Tokyo, Japan). Vickers hardness (*H*v) tests of the sintered blocks were performed on the sintered samples using a Vickers single crystalline diamond indenter (THVS-10/30/50MDX-AXY, Shanghai Teshi Precision Instrument Co., Ltd., Shanghai, China). The Vickers hardness was calculated using the following equation (2):

$$Hv = 1854.4 \times F/L^2 \quad (2)$$

where F represents the applied load, and L is the arithmetic mean of the two diagonals of the Vickers indentation.[37]

RESULTS AND DISCUSSION

Characterization of the Fe_2O_3 raw material. The scanning electron microscopy (SEM) results, as shown in Fig. 1a, reveal that the 30 nm α-Fe_2O_3 raw material exhibits an agglomerated state, with particle clusters ranging from several to dozens of micrometers in diameter. At higher magnification (Fig. 1b, 1c), these agglomerates are clearly visible as loose assemblies composed of nanoscale components. The fine particle size of the raw material enhances the homogeneity of the chemical composition in the final sintered body, resulting in excellent phase structure uniformity and sufficient density.

Elemental analysis indicates that the main impurity elements in the nano-Fe_2O_3 powder include: 0.36% Na_2O, 0.0078% MgO, 0.016% Al_2O_3, 0.015% K_2O, 0.22% CaO, 0.00071% TiO_2, 0.0032% MnO, and 26.4 μg g^{-1} Cr. To investigate the potential influence of matrix elements, particularly trace chromium, on iron isotope measurements, comparative experiments were conducted with and without iron isotope separation and purification after powder digestion. The comparative results are presented in a three-isotope plot (Fig. 2). The gradient of the δ^{56}Fe and δ^{57}Fe fractionation line is 1.481 ± 0.009, which aligns within error margins with both equilibrium (1.475) and kinetic (1.488) fractionation slopes. The isotope fractionation trend indicates the absence of analytical artifacts caused by unresolved isobaric interferences. The Fe component exhibits consistent behavior regardless of whether separation steps were employed in the analytical process. This aligns with previous research findings,[33] confirming that these low-level matrix elements do not significantly interfere with iron

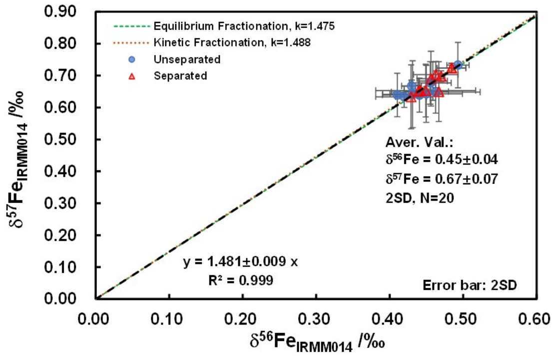

Fig. 2 Plot of $\delta^{56}Fe_{IRMM014}$ vs $\delta^{57}Fe_{IRMM014}$ of 30 nm α-Fe_2O_3 powder. Red triangles represent samples that underwent chemical separation; blue dots represent samples that did not. All data define a linear trend with a slope of 1.481 ± 0.009, which is close to both the theoretical equilibrium fractionation value (1.475) and the kinetic fractionation value (1.488).

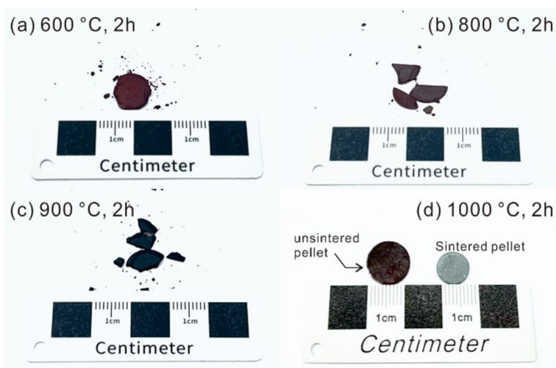

Fig. 3 Hematite pellets sintered for 2 hours at different temperatures: (a) 600 °C, (b) 800 °C, (c) 900 °C, and (d) 1000 °C. At 1000 °C, the sintered hematite exhibits significant volume shrinkage without cracking.

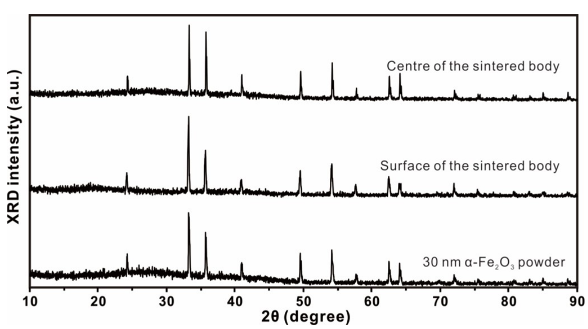

Fig. 4 XRD patterns of sintered hematite (center and surface) compared with the original 30 nm α-Fe_2O_3, showing identical diffraction peaks.

isotope determination. The influence of matrix elements and chromium present in the selected nano-Fe_2O_3 powder on iron isotope measurements can be considered negligible, eliminating the need for subsequent separation, purification, or elemental interference corrections in the preparation of iron isotope reference materials.

Selection of the sintering temperature. The mechanical strength of the bulk samples is significantly influenced by the sintering temperature. To determine the optimal sintering temperature, a series of experiments were conducted at different temperatures (600°C, 800°C, 900°C, and 1000°C), with each temperature maintained for 2 hours. As shown in Fig. 3, samples sintered at 600°C, 800°C, and 900°C exhibited distinct brittle characteristics (Fig. 3a-c). When the sintering temperature was increased to 1000°C, the samples underwent significant volumetric shrinkage, displaying smooth and intact edges, while their color transformed from the initial brick-red to dark gray (Fig. 3d). These samples demonstrated excellent ductility and significantly enhanced density. These macroscopic observations strongly correlate with SEM analysis results, which revealed numerous pores and cracks in the directly compressed powder compacts (Fig. 1d). These microstructural defects substantially reduced the material's mechanical properties, making the samples prone to fragmentation. In the state of insufficient particle contact, the samples maintained a brick-red appearance similar to that of nano-Fe_2O_3 powder.

During atmospheric pressure solid-phase sintering, high-temperature-driven mass transport primarily occurs through surface diffusion and grain boundary diffusion mechanisms. These diffusion processes facilitate the formation of "neck" structures[38,39] between nano-Fe_2O_3 particles, which gradually expand as sintering progresses, ultimately achieving effective particle interconnection while simultaneously closing and eliminating pores. Under the high temperature of 1000°C, Fe_2O_3 particles underwent significant surface diffusion, forming stable neck connections at grain boundaries. Particle edges become blunted showing a clear tendency toward spheroidization (Fig. 1e). SEM observation of the polished surface (Fig. 1f) further confirmed that the original nanoparticles had fully consolidated, with significantly reduced porosity and substantially improved density. These microstructural improvements directly manifested in macroscopic properties: the sintered body not only exhibited notable volume shrinkage but also possessed sufficient mechanical strength to withstand subsequent washing and polishing treatments without cracking or fragmentation. Based on these experimental results, we determined the optimal sintering process parameters to be 1000°C for 2 hours.

Characterization of Fe_2O_3 powder and pellets. To investigate the potential effects of binder addition and high-temperature sintering on the samples, we conducted powder XRD analysis on the original nanopowder and micro-area XRD analysis on both the directly pressed powder pellet and the pellet after sintering (Fig. 4). A thorough examination of the analytical data revealed consistent outcomes across all three samples, indicating that neither binder addition nor high-temperature sintering significantly altered the material's phase composition. The average Vickers hardness was measured to be approximately 228.31 ± 3.77 *H*v when applying a loading force of ~0.5 kg, suggesting that the pellet exhibits hardness

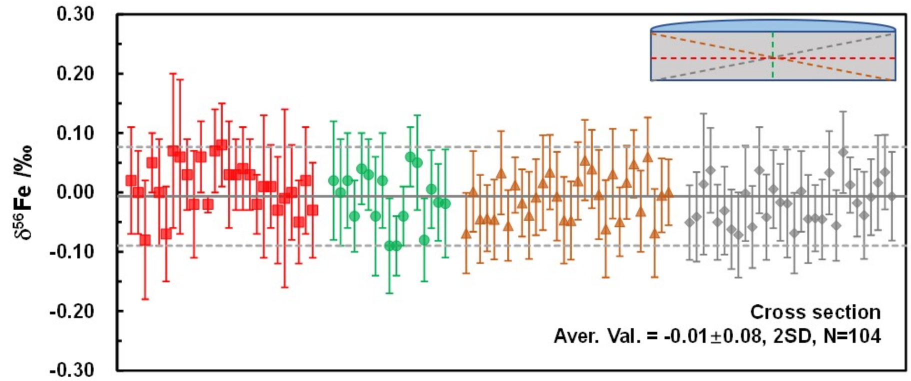

Fig. 5 Homogeneity of $\delta^{56}Fe$ measurements across a cross-section of sintered hematite. Colors correspond to different orientations of analysis points. A randomly selected sintered hematite sample was used as a bracketing standard. Error bars represent 2SE for individual points.

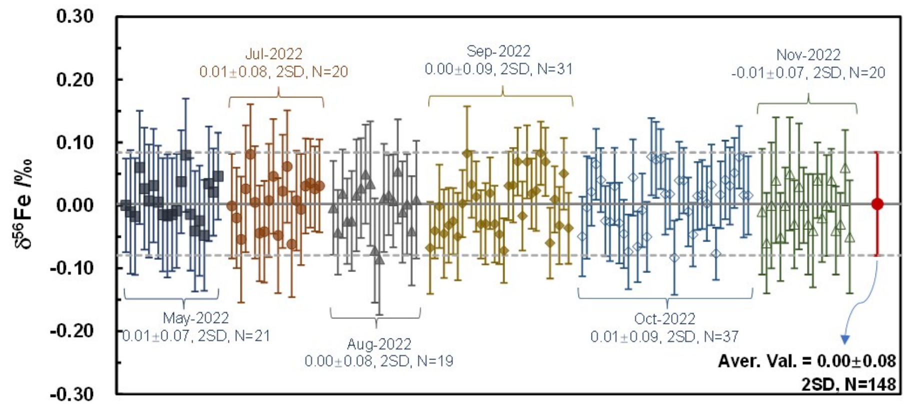

Fig. 6 Long-term homogeneity and stability of $\delta^{56}Fe$ measurements on the surface of sintered hematite over six months, obtained using fsLA-MC-ICP-MS. Different colors represent data points from each month. A randomly selected sintered hematite sample was used as a bracketing standard. Error bars represent 2SE for individual points and 2SD for average values.

comparable to that of stainless steel. These findings demonstrate that the preparation strategy effectively preserves the inherent properties of the material while significantly enhancing its hardness. Therefore, this method optimally retains the desired attributes of the sample, making it a promising approach for material preparation in this context.

Homogeneity of Fe isotopic composition in sintered hematite. This study systematically analyzed samples of sintered hematite, heat-treated at 1000 °C for 2 h, using LA-MC-ICP-MS technology to evaluate the internal homogeneity of Fe isotopic composition. As shown in Fig. 5, cross-sectional measurements of Fe isotope ratios were performed along different marked lines, with a randomly selected sintered hematite sample serving as the reference standard. The results revealed that the $\delta^{56}Fe$ values of the sintered hematite ranged from –0.09‰ to 0.08‰, with an average of –0.01 ± 0.08‰ (2SD, n=104). This finding aligns with the sample's dense and homogeneous morphological characteristics, confirming the suitability of sintered hematite as a reference material for *in-situ* Fe isotopic determination.

A six-month long-term tracking study was conducted to systematically assess the homogeneity and stability of the sintered hematite. To eliminate potential temporal and batch effects, samples were selected using a stratified random sampling method from different production batches. A prepared hematite sample was used as an internal standard during the Fe isotopic ratio measurements of the randomly selected sample batches to minimize matrix effects (Fig. 6). The results showed $\delta^{56}Fe$ values for different batches as follows: 0.01 ± 0.07‰ (2SD, n=21); 0.00 ± 0.08‰ (2SD, n=19); 0.00 ± 0.09‰ (2SD, n=31); 0.01 ± 0.09‰ (2SD, n=37); and –0.01 ± 0.07‰ (2SD, n=20). The $\delta^{56}Fe$ variations across all tested samples did not exceed 0.1‰, demonstrating excellent reproducibility. These results confirm the outstanding Fe isotopic homogeneity and long-term stability of the sintered hematite samples.

The impact of the sintering process on Fe isotopic composition was examined by analyzing the original powder and samples from various preparation stages using solution-based Fe isotope analysis. As shown in Fig. 7, the initial nano-Fe_2O_3 powder exhibited a $\delta^{56}Fe_{IRMM014}$ value of 0.45 ± 0.04‰ (2SD, N=20). The pressed pellets had a $\delta^{56}Fe_{IRMM014}$ value of 0.45 ± 0.02‰ (2SD, n=3), while the sintered pellets yielded a value of 0.44 ± 0.04‰

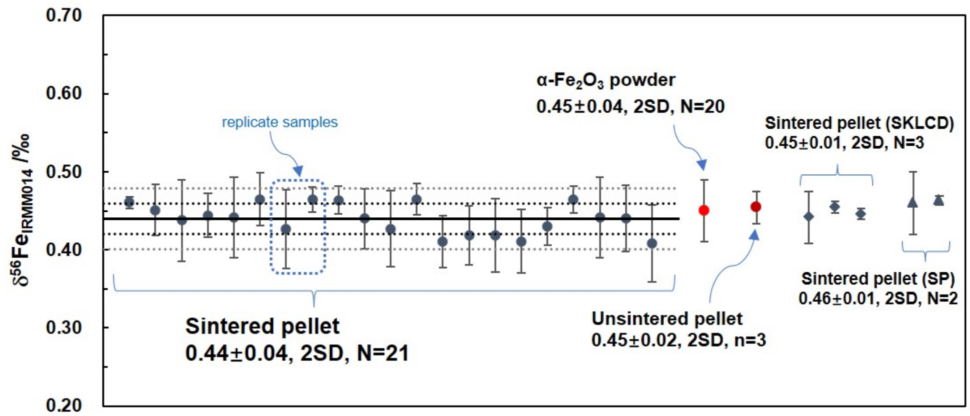

Fig. 7 $\delta^{56}Fe_{IRMM014}$ measurements of sintered and unsintered pellets, as well as the original 30 nm α-Fe_2O_3 powder, acquired using SN-MC-ICP-MS. The data show consistency within the acceptable error range. Error bars represent 2SE for individual points and 2SD for average values. N represents the total number of samples analyzed; n denotes the number of tests per individual sample.

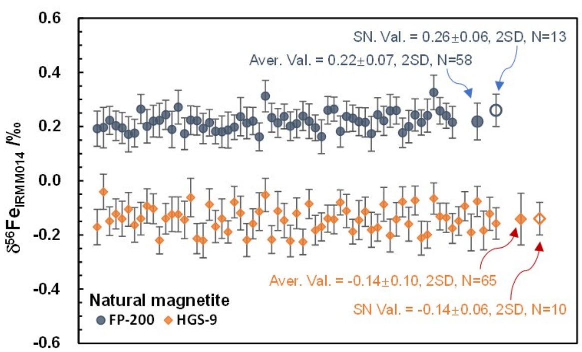

Fig. 8 Fe isotopic data of two natural magnetite reference materials, FP-200 and HGS-9, acquired by LA-MC-ICP-MS using the sintered hematite reference material as an external standard. Error bars represent 2SE for individual points and 2SD for average values.

(2SD, N=21). These results indicate that the Fe isotopic composition remained consistent throughout the preparation process, validating the reliability of the method and confirming its robustness in producing matrix-matched reference materials.

To further validate the stability of the Fe isotopic composition in sintered hematite samples, five samples were randomly selected from 100 sintered bodies and analyzed by two independent laboratories. The State Key Laboratory of Continental Dynamics at Northwest University analyzed three samples using direct MC-ICP-MS measurements after sample digestion, obtaining $\delta^{56}Fe_{IRMM014}$ values of 0.45 ± 0.01‰ (2SD, N=3). Wuhan Sample Solution Analytical Technology Co., Ltd. analyzed two samples by first performing Fe isotope separation and purification after digestion, followed by MC-ICP-MS measurements, yielding $\delta^{56}Fe_{IRMM014}$ values of 0.46 ± 0.01‰ (2SD, N=2). Despite the different sample processing procedures employed by the two laboratories (direct measurement vs. separation and purification), the results exhibited high consistency. This not only confirms the homogeneity of the samples' Fe isotopic composition but also verifies the excellent interlaboratory comparability of the analytical results. These findings indicate that the prepared sintered hematite samples are reliable Fe isotopic reference materials.

Analytical verification of sintered hematite as a reference material. To evaluate the feasibility of using sintered hematite as a reference material, we selected two natural magnetite crystals with known iron isotopic compositions (FP-200 and HGS-9) as test samples. These samples, collected from Fuping County in Hebei Province and the Huanggangshan tin-polymetallic deposit in Inner Mongolia, China, respectively, are newly developed natural homogeneous reference materials for magnetite iron isotope analysis.[40]

In the *in-situ* Fe isotope analyses using sintered hematite as the external standard, the $\delta^{56}Fe_{IRMM014}$ values for FP-200 and HGS-9 were determined to be 0.22 ± 0.07‰ (2SD, n=58) and -0.14 ± 0.10‰ (2SD, n=65), respectively (Fig. 8). These results are in excellent agreement with previously reported solution method values (FP-200: 0.26 ± 0.06‰; HGS-9: -0.14 ± 0.06‰).[40]

The strong consistency between the *in-situ* measurements and the solution method data not only validates the reliability of the analytical method but also confirms the good homogeneity and stability of the sintered hematite samples studied. This stability across different analytical techniques (*in-situ* vs. solution methods) and sample types (sintered hematite vs. natural magnetite) underscores the reliability of this reference material, indicating that it can serve as a standard reference material for iron isotope geochemical research.

CONCLUSION

This study successfully established an efficient method for preparing hematite reference materials for *in-situ* iron isotope analysis using LA-MC-ICP-MS, utilizing nano-Fe_2O_3 powder. Repeated tests with solution methods and LA-MC-ICP-MS have verified that this method can stably achieve precision and accuracy better than 0.1‰. The prepared sintered pellets exhibit advantages such as stable storage, easy polishing, simple operation, and strong resistance to contamination. This method offers an innovative strategy for preparing solid reference materials, particularly suitable for isotopic systems that currently lack isotopically homogeneous, matrix-matched standard materials at the microscale. By optimizing the sintering process, this method achieves a perfect combination of high density and fine homogeneity in the reference material. This innovative approach holds significant value in the preparation of matrix-matched standard materials for LA-MC-ICP-MS analysis in the field of Earth sciences. Its excellent applicability and product quality will significantly enhance the accuracy and reliability of geochemical analyses, providing strong technical support for related research.

AUTHOR INFORMATION

Ming Li is a senior engineer at the State Key Laboratory of Geological Processes and Mineral Resources, China University of Geosciences (Wuhan), China. He obtained his Ph.D. in geochemistry from the China University of Geosciences (Wuhan) in 2010. His primary research interests encompass analytical geochemistry, geochemical microanalysis, and metal stable isotope analysis. As the lab manager of the Nu Plasma 1700 MC-ICP-MS facility, Dr. Li oversees the operation and management of the instrument and develops analytical methods for metal stable isotope analysis.

Corresponding Author

*M. Li

Email address: liming19820426@163.com

Notes

The authors declare no competing financial interest.

ACKNOWLEDGMENTS

This research was co-supported by the National Key R&D Programs of China (2019YFA0708401), the Natural Science Foundation of Hubei Province (2020CFA045), and the special fund from the State Key Laboratory of Geological Processes and Mineral Resources, China University of Geosciences (Wuhan).

REFERENCES

1. X. Zhu, R. K. O'Nions, Y. Guo, and B. C. Reynolds, *Science*, 2000, **287**, 2000-2002. https://doi.org/10.1126/science.287.5460.2000
2. X. Zhu, Y. Guo, R. K. O'Nions, E. D. Young, and R. D. Ash, *Nature*, 2001, **412**, 311-313. https://doi.org/10.1038/35085525
3. A. D. Anbar, J. E. Roe, J. Barling, and K. H. Nealson, *Science*, 2000, **288**, 126-128. https://doi.org/10.1126/science.288.5463.126
4. B. L. Beard and C. M. Johnson, *Geochim. Cosmochim. Acta.*, 1999, **63**, 1653-1660. https://doi.org/10.1016/S0016-7037(99)00089-7
5. C. M. Johnson, E. E. Roden, S. A. Welch, and B. L. Beard, *Geochim. Cosmochim. Acta.*, 2005, **69**, 963-993. https://doi.org/10.1016/j.gca.2004.06.043
6. F. von Blanckenburg, M. Mamberti, R. Schoenberg, B. S. Kamber, and G. E. Webb, *Chem. Geol.*, 2008, **249**, 113-128. https://doi.org/10.1016/j.chemgeo.2007.12.001
7. Z. Zhu, S. Jiang, R. Mathur, N. J. Cook, T. Yang, M. Wang, L. Ma, and C. L. Ciobanu, *Geochim. Cosmochim. Acta.*, 2018, **222**, 94-116. https://doi.org/10.1016/j.gca.2017.10.001
8. J. Torrent and U. Schwertmann, *J. Sediment. Res.*, 1987, **57**, 682-686. https://doi.org/10.1306/212F8BD4-2B24-11D7-8648000102C1865D
9. O. Bábek, M. Faměra, J. Hladil, J. Kapusta, H. Weinerová, D. Šimíček, L. Slavík, and J. Ďurišová, *Sediment. Geol.*, 2018, **364**, 71-88. https://doi.org/10.1016/j.sedgeo.2017.12.007
10. D. Tang, J. Ma, X.Y. Shi, M. A. Lechte, and X.Q. Zhou, *Am. Mineral.*, 2020, **105**, 1412-1423. https://doi.org/10.2138/am-2020-7406
11. C. M. Johnson and B. L. Beard, *Int. J. Mass Spectrom.*, 1999, **193**, 87-99. https://doi.org/10.1016/S1387-3806(99)00158-X
12. X.-Y. Zheng, B. L. Beard, and C. M. Johnson, *J. Anal. At. Spectrom.*, 2018, **33**, 68-83. https://doi.org/10.1039/C7JA00272F
13. N. Dauphas, P. R. Craddock, P. D. Asimow, V. C. Bennett, A. P. Nutman, and D. Ohnenstetter, *Earth Planet. Sci. Lett.*, 2009, **288**, 255-267. https://doi.org/10.1016/j.epsl.2009.09.029
14. N. S. Belshaw, X. K. Zhu, Y. Guo, and R. K. O'Nions, *Int. J. Mass Spectrom.*, 2000, **197**, 191-195. https://doi.org/10.1016/S1387-3806(99)00245-6
15. N. Dauphas, P. R. Craddock, P. D. Asimow, V. C. Bennett, A. P. Nutman, and D. Ohnenstetter, *Earth Planet. Sci. Lett.*, 2009, **288**, 255-267. https://doi.org/10.1016/j.epsl.2009.09.029
16. J. de Jong, V. Schoemann, J.-L. Tison, S. Becquevort, F. Masson, D. Lannuzel, J. Petit, L. Chou, D. Weis, and N. Mattielli, *Anal. Chim. Acta.*, 2007, **589**, 105-119. https://doi.org/10.1016/j.aca.2007.02.055
17. D. Malinovsky, A. Stenberg, I. Rodushkin, H. Andren, J. Ingri, B. Öhlander, and D. C. Baxter, *J. Anal. At. Spectrom.*, 2003, **18**, 687-695. https://doi.org/10.1039/B302312E
18. L. Xu, W. Zhang, T. Luo, J. Yang, and Z. Hu, *J. Anal. At. Spectrom.*, 2021, **36**, 747-757. https://doi.org/10.1039/D0JA00465K
19. M. Lazarov and I. Horn, *Spectrochim Acta B*, 2015, **111**, 64-73. https://doi.org/10.1016/j.sab.2015.06.013
20. S. Zhang, M. He, Z. Yin, E. Zhu, W. Hang, and B. Huang, *J. Anal. At. Spectrom.*, 2016, **31**, 358-382. https://doi.org/10.1039/C5JA00273G

21. T. Hirata, Y.Hayano, and T. Ohno, *J J. Anal. At. Spectrom.*, 2001, **16**, 487-491. https://doi.org/10.1039/B305127G
22. L. Xu, J. Yang, L. Xie, H. Wang, Y. Yang, C. Huang, and S. Wu, *Spectrochim Acta B*, 2022, **189**, 106374. https://doi.org/10.1016/j.sab.2022.106374
23. Y. He, S. Ke, F. Teng, T. Wang, H. Wu, Y. Lu, and S. Li, *Geostand. Geoanal. Res.*, 2015, **39**, 341-356. https://doi.org/10.1111/j.1751-908X.2014.00304.x
24. C. González de Vega, S. M. Chernonozhkin, R. Grigoryan, M. Costas-Rodríguez, and F. Vanhaecke, *J. Anal. At. Spectrom.*, 2020, **35**, 2517-2529.https://doi.org/10.1039/D0JA00225A
25. P. R. Craddock and N. Dauphas, *Geostand. Geoanal. Res.*, 2011, **35**, 101-123. https://doi.org/10.1111/j.1751-908X.2010.00085.x
26. C. C. Wohlgemuth-Ueberwasser, C. Ballhaus, J. Berndt, V. Stotter née Paliulionyte, and T. Meisel, *Contrib. Mineral. Petrol.*, 2007, **154**, 607-617. https://doi.org/10.1007/s00410-007-0212-x
27. Y. Feng, W. Zhang, Z. Hu, Y. Liu, K. Chen, J. Fu, J. Xie, and Q. Shi, *J. Anal. At. Spectrom.*, 2018, **33**, 2172-2183. https://doi.org/10.1039/C8JA00305J
28. Y. Feng, W. Zhang, Z. Hu, T. Luo, M. Li, Y. Liu, H. Liu, and Q. Li, *J. Anal. At. Spectrom.*, 2022, **37**, 551-562. https://doi.org/10.1039/D1JA00392E
29. C. Ballhaus and P. N. Sylvester, *J. Petrol.*, 2000, **41**, 545-561. https://doi.org/10.1093/petrology/41.12.1831
30. P. D. P. Taylor, R. Maeck, and P. Debievre, *Int. J. Mass Spectrom.*, 1992, **121**, 111-125. https://doi.org/10.1016/0168-1176(92)80075-C
31. J. Li, K. Zong, Q. He, Z. Wang, and Z. Hu, *Journal of Nanjing University(Natural Sciences)*, 2021, **557**, 944-956. https://jns.nju.edu.cn/CN/10.13232/j.cnki.jnju.2021.06.004
32. M. Li, Y. Lei, L. Feng, Z. Wang, N. S. Belshaw, Z. Hu, Y. Liu, L. Zhou, H. Chen, and X. Chai, *J. Anal. At. Spectrom.*, 2018, **33**, 1707-1719. https://doi.org/10.1039/C8JA00234G
33. Y. Lei, M. Li, Z, Wang, Y. Zhu, Z, Hu, Y, Liu and X, Chai, *Atom. Spectrosc.*, 2022, **43**, 214-222. https://doi.org/10.46770/as.2022.111
34. F. Lacan, L. Artigue, J. K. Klar, C. Pradoux, J. Chmeleff, and R. Freydier, *Front. Environ. Chem.*, 2021, **2**, 692025. https://doi.org/10.3389/fenvc.2021.692025
35. W. Zhang and Z. Hu, *Spectrochim Acta B*, 2020, **171**, 105929. https://doi.org/10.1016/j.sab.2020.105929
36. W. Zhang, Z. Hu, and Y. Liu, *J. Anal. At. Spectrom.*, 2020, **35**, 1087-1096. https://doi.org/10.1039/D0JA00084A
37. W. Sun, X. Kuang, H. Liang, X. Xia, Z. Zhang, C. Lu, and A. Hermann, *Phys. Chem. Chem. Phys.*, 2020, **22**, 5018-5023. https://doi.org/10.1039/C9CP06819H
38. M. Wu, L. Chang,Y. Cui, X. Chen, X. He, and X. Qu, *Chinese Journal of Engineering*, 2014, **36**, 345-353. https://cje.ustb.edu.cn/cn/article/doi/10.13374/j.issn1001-053x.2014.03.011
39. C. Yu, G. Xing, Z. Wu, B. Dong, J. Ding, J. Di, H. Zhu, and C. Deng, *Chinese Journal of Materials Research*, 2022, **36**, 679-686. https://doi.org/10.11901/1005.3093.2021.172
40. Y. Feng, W. Zhang, Y. Bao, X. Zeng, H. Liu, T. Luo, Z. Hu, M. Zhang, Y. Wang, Y. Yang, and S. Liu, *Geostand. Geoanal. Res.*, 2024, online published. https://doi.org/10.1111/ggr.12592